Characterization of Impurity Doping and Stress in Si/Ge and Ge/Si Core–Shell Nanowires

Naoki Fukata,[†,*] Masanori Mitome,[†] Takashi Sekiguchi,[†] Yoshio Bando,[†] Melanie Kirkham,[‡,#] Jung-Il Hong,[§,‡] Zhong Lin Wang,[‡,†] and Robert L. Snyder[‡,⊥]

[†]International Center for Materials Nanoarchitectonics, National Institute for Materials Science, 1-1 Namiki, Tsukuba, 305-0044, Japan, [‡]School of Materials Science and Engineering, Georgia Institute of Technology, Atlanta, Georgia 30332-0245, United States, and [§]Daegu Gyeongbuk Institute of Science and Technology (DGIST), Daegu, Korea. [#]Present address: Materials Science & Technology Division, Oak Ridge National Laboratory, Oak Ridge, TN 37831–6064, United States. [⊥]Deceased.

ABSTRACT Core–shell nanowires (NWs) composed of silicon (Si) and germanium (Ge) are key structures for realizing high mobility transistor channels, since the site-selective doping and band-offset in core–shell NWs separate the carrier transport region from the impurity doped region, resulting in the suppression of impurity scattering. Four different types of Si/Ge (i-Si/n-Ge, p-Si/i-Ge) and Ge/Si (n-Ge/i-Si, i-Ge/p-Si) core–shell NWs structures were rationally grown. The surface morphology significantly depended on the types of the core–shell NWs. Raman and X-ray diffraction (XRD) measurements clearly characterized the compressive and tensile stress in the core and shell regions. The observation of boron (B) and phosphorus (P) local vibrational peaks and the Fano effect clearly demonstrated that the B and P atoms are selectively doped into the shell and core regions and electrically activated in the substitutional sites, showing the success of site-selective doping.

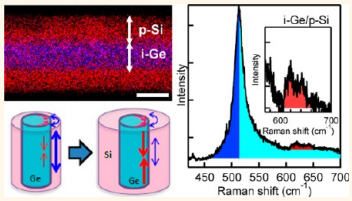

KEYWORDS: core–shell nanowires · doping · X-ray diffraction · Raman scattering

Technical progress in silicon very large scale integrated circuits (Si VLSIs) has so far been driven by the miniaturization, or scaling, of gates, oxide layers, p–n junctions, and other elements in metal-oxide semiconductor field-effect transistors (MOSFETs), the building blocks of VLSIs. However, potential advances in performance and integration by conventional scaling of device geometries are now reaching their practical limits. To overcome these limiting factors in planar MOSFETs, vertical structural arrangements using semiconductor nanowires (NWs) have been suggested as the basis for the next generation of semiconductor devices. Considerable work has been done regarding one-dimensional semiconductor nanowires.[1–8] Silicon (Si) and germanium (Ge) NWs have attracted special attention, due to their compatibility with current Si complementary metal-oxide semiconductor (Si CMOS) integrated circuit technology and their better scalability and leakage control.

Impurity doping is necessary to form source and drain regions in NWs-MOSFETs, while the retardation of carrier mobility due to impurity scattering has to be taken into account when doping the channel region. Core–shell NWs using Si and Ge show potential for suppression of impurity scattering. Following a pioneering work by Lauhon *et al.* on the growth of Si/Ge core–shell NWs,[9] numerous studies have been carried out, both experimentally and theoretically.[10–19] Impurities are doped in the core and free carriers are injected into the shell, or *vice versa*. In this study, doped impurities and carriers are separated in the core and shell regions, respectively, due to the band offset between Si and Ge, resulting in a markedly low scattering rate between them and improved mobility of free carriers. High hole mobility has, in fact, been reported in top-gated Ge/Si NWFET devices.[10] Stress also plays an important role in carrier mobility, since it lifts the band-edge degeneracies that affect the transport masses and reduces intervalley or interband scattering.[20,21] Estimation of stress in the core and shell regions in core–shell NWs is, therefore, also important. Stress in Ge/Si core–shell NWs with thin Si shells of about 3 nm has been investigated by Goldthorpe *et al.* by transmission electron microscopy (TEM) and Raman measurements.[12,13] The authors also showed relationships between axial strain and dislocation density in the Ge core of core–shell NWs with various core diameters and shell thicknesses.

Characterization of impurity atoms selectively doped in the core and shell regions of Si/Ge and Ge/Si core–shell NWs is necessary

* Address correspondence to FUKATA.Naoki@nims.go.jp.

Received for review June 28, 2012 and accepted September 1, 2012.

Published online September 05, 2012
10.1021/nn302881w

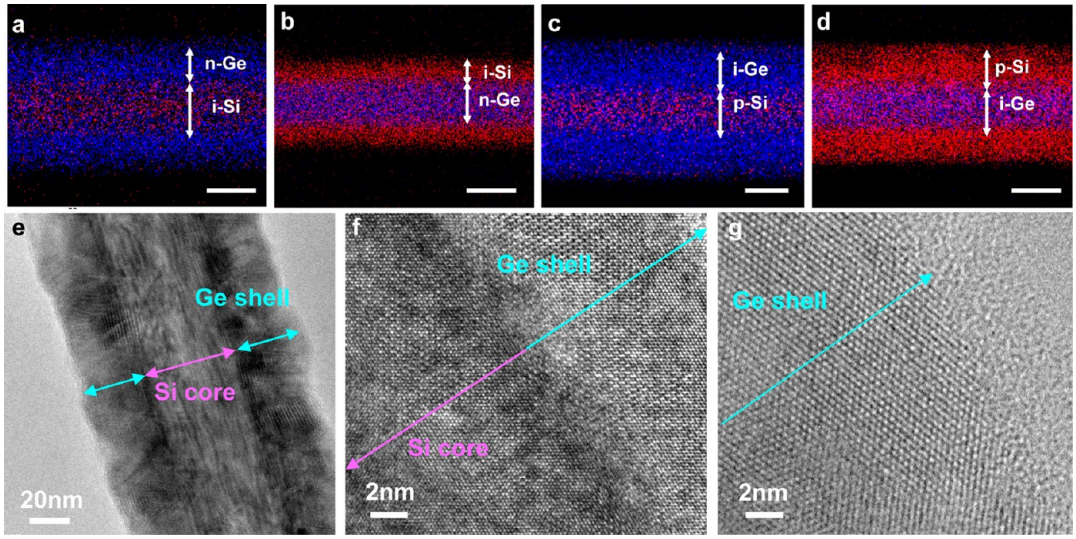

Figure 1. EDX images of (d) i-Si/n-Ge, (e) n-Ge/i-Si, (f) p-Si/i-Ge, and (g) i-Ge/p-Si core−shell NWs. The scale bar is 30 nm. The red represents Si and blue represents Ge. Illustrations of band diagrams of four different types of core−shell NWs are shown as insets. TEM images of i-Si/n-Ge are shown in panels e−g.

to arrive at an understanding of the states and behaviors of dopant atoms and thence to control the doping levels. Raman scattering is a useful technique in this regard.[22−24] It is also possible to evaluate the stress in core−shell NWs by investigating the peak shifts of the Si and Ge optical phonon peaks. X-ray diffraction (XRD) is also a powerful method[12,13] for characterizing core−shell NWs with larger diameters.

In this paper, we report the growth of four different types of Si/Ge and Ge/Si core−shell NWs and selective doping in the core and shell regions. The Raman measurements clarified the status of impurity atoms. These results clearly showed the bonding states and the electrical activities of impurity atoms, demonstrating the formation of n-shell and p-shell layers. The stress in the core and shell regions was evaluated by XRD and Raman measurements, which revealed the major influence of shell thickness. XRD measurements also clearly showed lattice contraction caused by impurity doping.

RESULTS AND DISCUSSION

Four different types of Si/Ge (i-Si/n-Ge, p-Si/i-Ge) and Ge/Si (n-Ge/i-Si, i-Ge/p-Si) core−shell NWs were prepared by CVD to realize the band structures illustrated in the insets of Figure 1. To confirm the formation of Si/Ge and Ge/Si core−shell NWs, EDX measurements were first performed during TEM measurements. The results obtained for a shell growth time of 30 s are shown in Figure 1a−d. The red represents Si and blue represents Ge. These results clearly show the formation of Si/Ge and Ge/Si core−shell NWs. Almost all core NWs showed ⟨111⟩ orientation. We also carefully checked the crystallinity of the shell in Si/Ge and Ge/Si core−shell NWs and observed clear lattice fringes in the shell regions (Figure 1e−g). The TEM image of Figure 1e shows a slightly rough surface, similar to previous reports.[12] Evidence of shell crystallinity was also shown by the results of the XRD and Raman measurements described below.

The SEM images of typical i-Si/n-Ge core−shell NWs are shown in Figure 2a−c. The SEM images demonstrate that the diameter is uniform along the length of the core−shell NWs. The diameter significantly increases with an increase in the shell growth time. The surface is relatively smooth. The same results were obtained for n-Ge/i-Si and i-Ge/p-Si core−shell NWs. On the other hand, p-Si/i-Ge core−shell NWs showed very rough surfaces, as seen in Figure 2e−g. The introduction of B_2H_6 gas in SiH_4 gas enhances radial growth of the Si layer, giving SiNWs with tapered structures with significant surface doping.[25] This affects the surface roughness of p-SiNWs in the core region. To clarify it, we performed TEM measurements for i-SiNWs and p-SiNWs. The TEM images of i-SiNWs and p-SiNWs before the shell growth are shown in Figure 2d,h. In this study, we reduced the B_2H_6 gas flux to suppress the radial growth. However, the radial growth slightly occurred as shown in Figure 2h. The high resolution TEM image (Figure 2i) and the diffractograms (Fourier transform images) clearly show that the near surface region is polycrystalline. This affects the surface roughness for p-SiNWs. Finally, the surface roughness further increased after the formation of i-Ge shell (Figure 2e−g). Figure 2j shows a summary of the thickness of the shell layers in four different Si/Ge and Ge/Si core−shell NWs as a function of shell growth time. They are approximately linear with respect to the shell growth time, indicating that the thickness of the shell layer may be controllable by the shell growth time. The two different types of Si/Ge core−shell NWs, i-Si/n-Ge and p-Si/i-Ge, show almost the same behaviors.

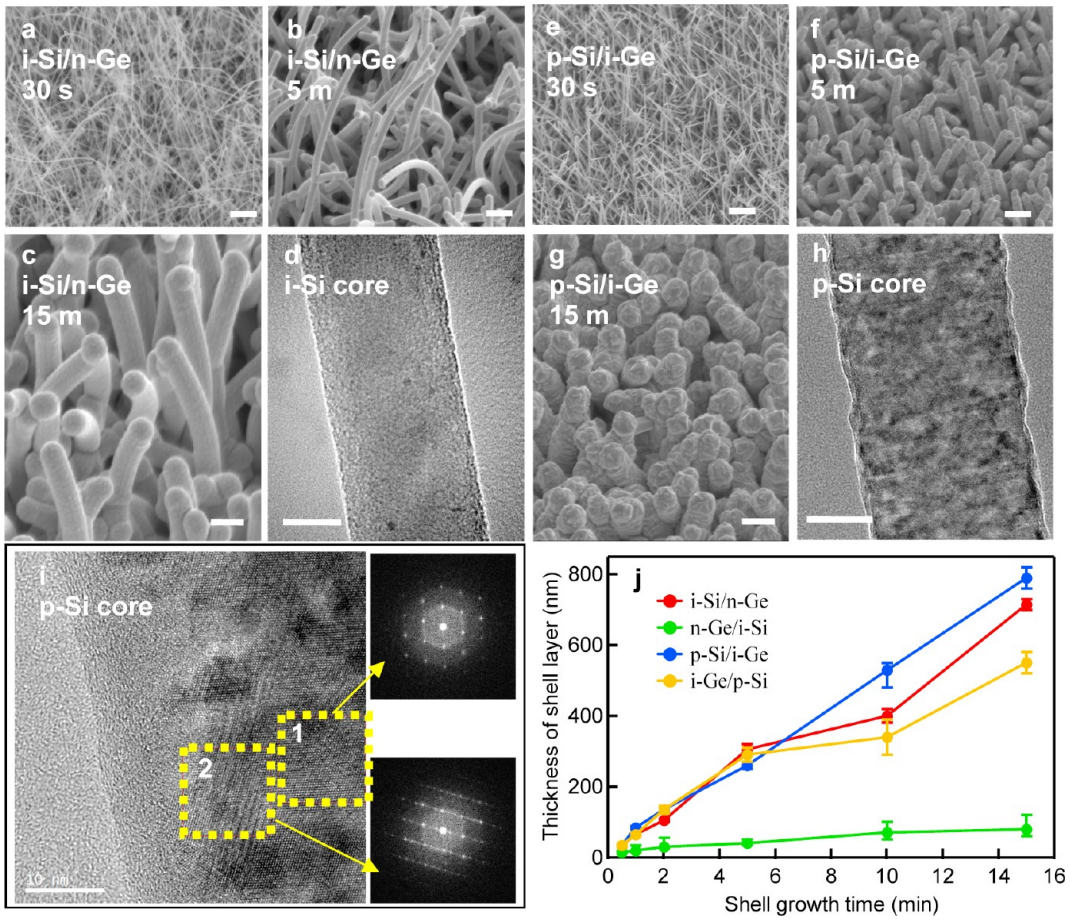

Figure 2. SEM images of i-Si/n-Ge core–shell NWs with shell growth time for (a) 30 s, (b) 5 min, and (c) 15 min. SEM image of p-Si/i-Ge core–shell NWs with shell growth time for (e) 30 s, (b) 5 min, and (g) 15 min. TEM images of (d) i-Si core and (h) p-Si core NWs. (i) High resolution TEM image of p-Si core NWs and diffractograms (Fourier transform images) in the center (1) and near surface (2) regions. (j) Dependence of the thickness of shell layers on the shell growth time for four different types of core–shell NWs. The scale bars of panels a–c and e–g are 2 μm. The scale bars of panels d and h are 30 nm.

On the other hand, the other two types of Ge/Si core–shell NWs (n-Ge/i-Si and i-Ge/p-Si) show different behaviors; that is, i-Ge/p-Si shows closely similar behavior to the Si/Ge core–shell NWs series, and n-Ge/i-Si shows a weak dependence on the shell growth time, which can be explained by the fact that radial growth of the Si shell on GeNWs is more difficult to achieve than that of the Ge shell layer on SiNWs. The radial growth of i-Ge/p-Si core–shell NWs is much faster than that of n-Ge/i-Si core–shell NWs, in spite of the shell being composed of Si. This is due to the enhancement radial growth by B_2H_6 gas.

Stress and the doping effect in Si/Ge and Ge/Si core–shell NWs were evaluated by XRD measurements. The dependence of XRD patterns on the shell growth time, observed for four different structures, is shown in Figure 3. The results show peaks representing the (111) crystallographic planes of the diamond cubic structures of Ge and Si, indicating that both core and shell regions are crystalline. The atomic scattering factor for Ge is larger than that for Si (~26.5 *vs* 10.4 at our conditions), which explains the low Si peak, relative to the Ge peak. We did a pattern simulation, and with an approximately equal mol % of Si and Ge, the Ge (111) peak will still be ~6 times larger than the Si (111) peak. In addition to this, all XRD patterns were normalized by the intensity of the Ge (111) peak in Figure 3. Therefore, the Si (111) peak becomes smaller relative to the Ge peak with increasing Ge shell growth time (Figure 3a,c), while the Si (111) peak becomes larger relative to the Ge peak with increasing Si shell growth time (Figures 3b,d). Both the Ge (111) and the Si (111) peaks clearly shift with increased shell growth time, indicating a shift in lattice constant.

Figure 4a shows the lattice constant results of the Si core in Si/Ge core–shell NWs. The average lattice constants of Ge and Si in the core–shell NWs were calculated by fitting the Ge and the Si-related XRD peaks. The average lattice constant of the Si core is greater than that for bulk Si and increases with increased shell growth time, showing that the tensile stress is applied by the radial growth of the Ge shell,

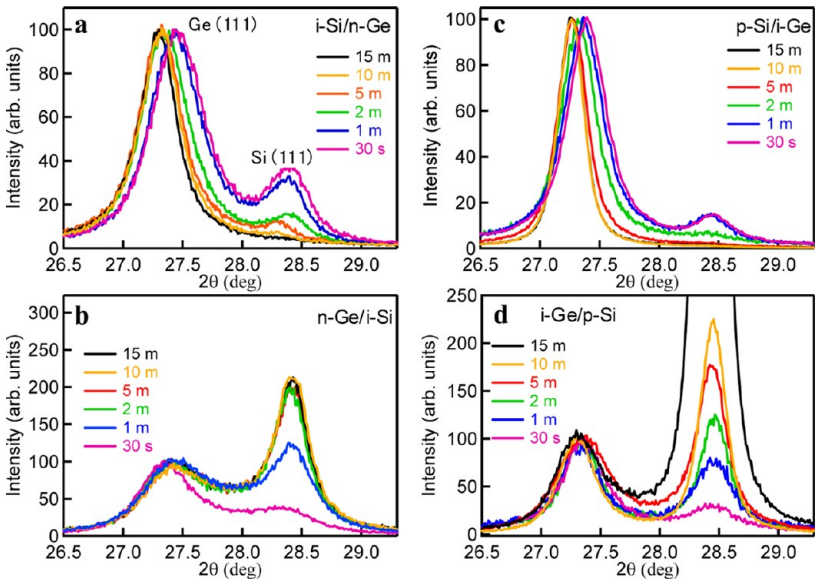

Figure 3. XRD spectra of Ge (111) and Si (111) peaks observed for (a) i-Si/n-Ge, (b) n-Ge/i-Si, (c) p-Si/i-Ge, and (d) i-Ge/p-Si core–shell NWs. The results show the dependence on the shell growth time.

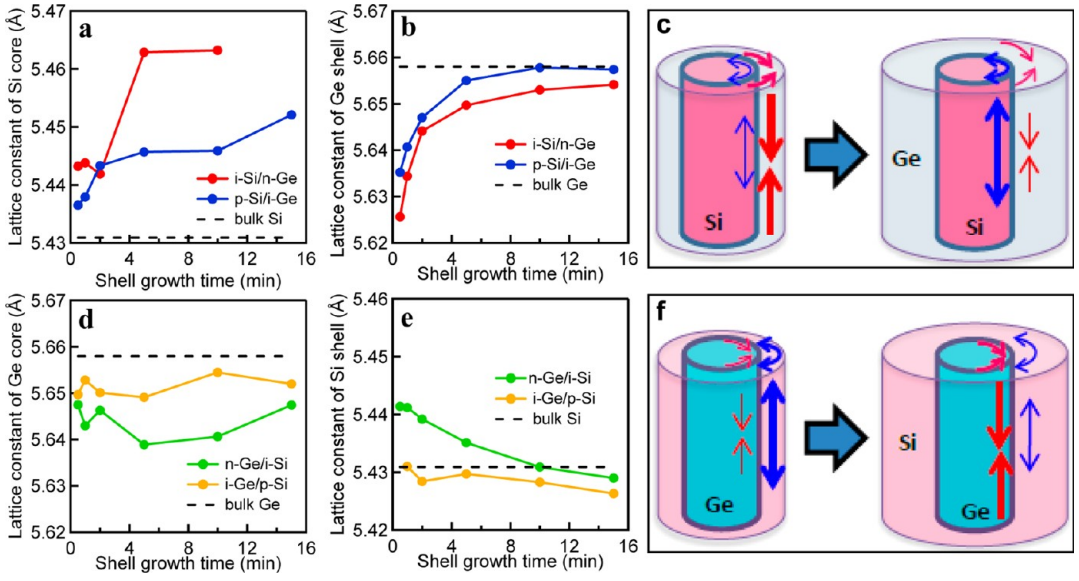

Figure 4. Dependence of the average lattice constant of four different core–shell NWs on the shell growth time. The lattice constant of (a) the Si core in the i-Si/n-Ge and p-Si/i-Ge core–shell NWs, (b) the Ge shell in the i-Si/n-Ge and p-Si/i-Ge core–shell NWs, (d) the Ge core in the n-Ge/i-Si and i-Ge/p-Si core–shell NWs, and (e) the Si shell in the n-Ge/i-Si and i-Ge/p-Si core–shell NWs. Schematic illustration of the stress induced by the formation of (c) Si/Ge and (f) Ge/Si core–shell NWs.

which increases with the thickness of the Ge shell. The average lattice constant of the Si core in p-Si/i-Ge is smaller than that in i-Si/n-Ge, showing that the lattice contraction of the Si core in p-Si/i-Ge could result from the substitution of B atoms into the Si lattice, indicating B-doping in the Si core region of p-Si/i-Ge. Figure 4b shows the results of the Ge shell in the Si/Ge core–shell NWs. The average lattice constant of the Ge shell is lower than that for bulk Ge and increases with increasing shell growth time, showing that compressive stress originates in the Si core but that its effect is weakened by increasing the Ge shell thickness. The average lattice constant of the Ge shell in i-Si/n-Ge is smaller than that in p-Si/i-Ge, demonstrating that lattice contraction of the Ge shell in i-Si/n-Ge might result from the substitution of P atoms into the Ge lattice, and indicating P-doping in the Ge shell region of i-Si/n-Ge. The relationship of the stress in the Si core and Ge shell regions in the Si/Ge core/shell NWs is illustrated in Figure 4c. Here, the thicker arrows indicate a higher stress. Figure 4d shows the results for the Ge core in the Ge/Si core–shell NWs. The average lattice constant of

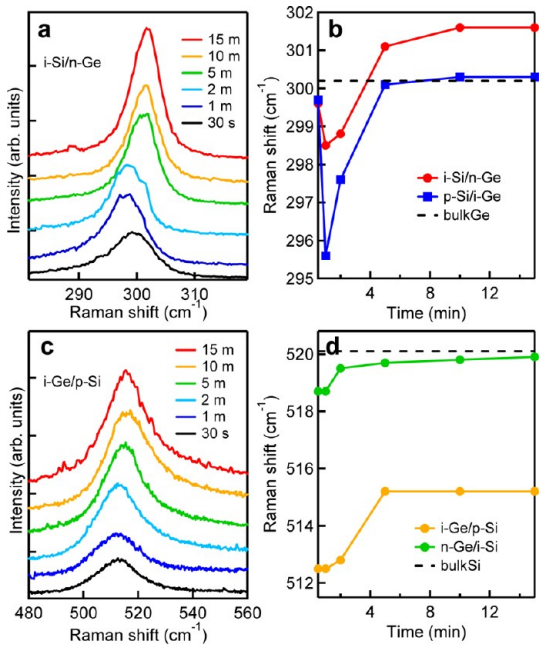

Figure 5. (a) Ge optical phonon peaks observed for i-Si/n-Ge core–shell NWs and (c) Si optical phonon peaks observed for i-Ge/p-Si core–shell NWs. Raman shift of (b) the Ge optical phonon peak and (d) the Si optical phonon peak as a function of the shell growth time.

the Ge core is lower than that for bulk Ge, showing that the compressive stress originates in the Si shell. The average lattice constant of the Ge core in n-Ge/i-Si is smaller than that in i-Ge/p-Si. This can also be explained by the fact that the lattice contraction of the Ge core in n-Ge/i-Si is caused by the substitution of P atoms into the Ge lattice, indicating P-doping in the Ge core region of n-Ge/i-Si. The dependences on the shell growth time for Ge/Si core–shell NWs (Figure 4d) are smaller than those for Si/Ge core–shell NWs (Figure 4b). This is probably attributable to relaxation caused by the radial growth of Ge/Si core–shell NWs being at a higher temperature (700 °C) than for the Si/Ge core–shell NWs (500 °C). Figure 4e shows the results for the Si shell in Ge/Si core–shell NWs. The average lattice constant of the Si shell for n-Ge/i-Si core–shell NWs is greater than that for bulk Si at the start of the shell growth time. It then reaches the bulk Si value, revealing that the tensile stress originates in the Ge core at the initial stage, and finally the Si shell is relaxed. The average lattice constant of the Si shell for n-Ge/i-Si core–shell NWs is also greater than that for i-Ge/p-Si core–shell NWs. This is attributable to the lattice contraction of the Si shell in i-Ge/p-Si being caused by the substitution of B atoms into the Si lattice, indicating B-doping in the Si shell region of i-Ge/p-Si. The stress relationship of the Ge core and Si shell regions in Ge/Si core–shell NWs is illustrated in Figure 4f.

The stress and doping effects in Si/Ge and Ge/Si core–shell NWs were also investigated by micro-Raman scattering measurements. Only the shell layers can be mainly characterized by Raman measurements, due to limits on the penetration depth of excitation laser light. We could observe an optical phonon peak related to Si–Ge bonds for core–shell NWs with thin shell layers (Figure S1). However, we could not get enough data to investigate stress and intermixing of Si and Ge atoms. The effect of intermixing will be discussed later. Figure 5a shows the results of the Ge optical phonon peaks observed for i-Si/n-Ge core–shell NWs as Raman spectra. The peak position significantly depends on the shell growth time. The dependence on shell growth time, in addition to the results for p-Si/i-Ge core–shell NWs, is summarized in Figure 5b. The Ge optical phonon peak initially decreased, then increased and finally reached a constant value. The initial decrease is due to the compressive stress applied by the Si core region, and the second increase is due to the decrease in effect of this compressive stress. Finally, the peak position of the Ge optical phonon peak observed for p-Si/i-Ge reached that for bulk Ge, indicating that the stress had been completely released. The Ge optical phonon peak for i-Si/n-Ge finally also shows a constant value, but at a higher position than for p-Si/i-Ge. This is also attributable to the substitution of P atoms into the Ge lattice, namely, lattice contraction resulting from P doping, and finally indicating P-doping in the Ge shell region of i-Si/n-Ge. These results are in good agreement with those obtained by XRD measurements.

The results of the shell layers in Ge/Si core–shell NWs are shown in Figure 5c,d. Figure 5c shows Si optical phonon peaks observed for i-Ge/p-Si core–shell NWs. The peak position also changes according to the shell growth time. The Si optical phonon peak shows a downshift due to tensile stress from the Ge core that shifts to lower wavenumbers with decreasing shell growth time, since a thinner Si shell layer is more affected by the Ge core. The results for n-Ge/i-Si show similar behavior, but with different peak positions. The peak position of the Si optical phonon peak for i-Ge/p-Si core–shell NWs is lower than that for n-Ge/i-Si. The lower frequency shift is caused by the Fano effect,[26,27] indicating B-doping in the Si shell region of i-Ge/p-Si. The Fano effect will be explained below.

To further confirm P and B doping in the shell layer of i-Si/n-Ge and i-Ge/p-Si core–shell NWs, we show the Raman spectra in Figure 6. Figure 6a shows the Ge optical phonon peak observed for i-Si/n-Ge core–shell NWs with a shell growth time of 15 min. A peak was observed at about 345 cm^{-1} in addition to the Ge optical phonon peak. The magnification is shown in Figure 6b. The peak position coincides with that of the P local vibrational mode in GeNWs,[23] showing that the peak can be assigned to the P local vibrational peak and that the P atoms have been doped into the

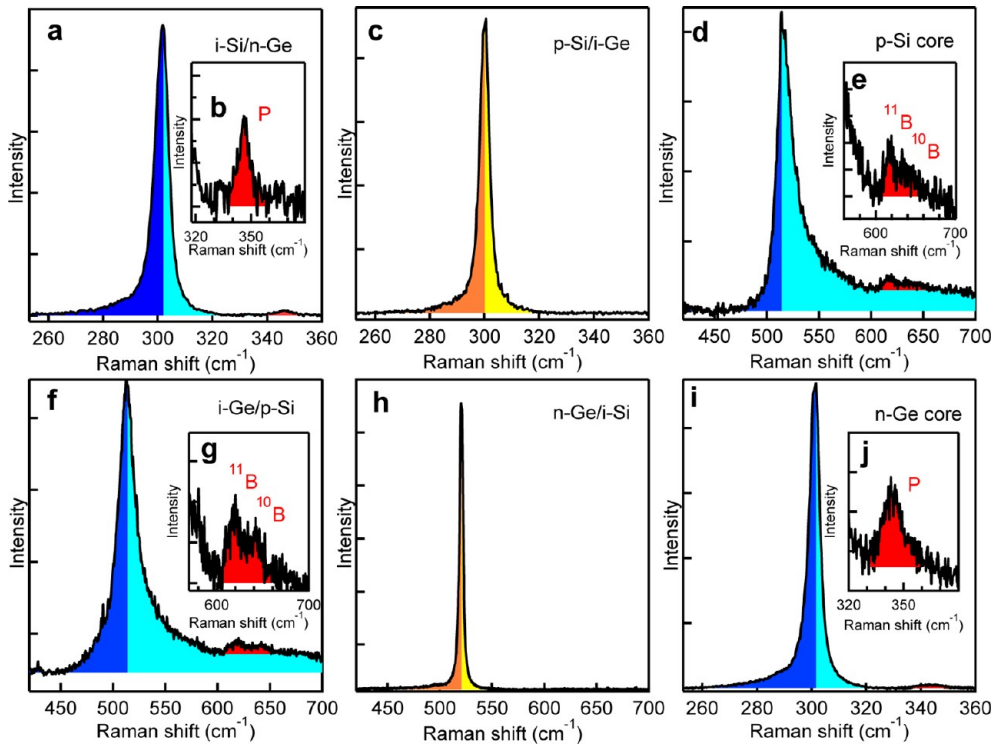

Figure 6. Raman spectra observed for (a) i-Si/n-Ge, (c) p-Si/i-Ge, (f) i-Ge/p-Si, and (h) n-Ge/i-Si core−shell NWs. Raman spectra observed for (d) p-Si core NWs and (i) n-Ge core NWs. Insets b and j are the magnification of the P local vibrational mode in the n-Ge shell layer and the n-Ge core, respectively. Insets g and e are the magnification of the ^{11}B and ^{10}B local vibrational peaks in the p-Si shell layer and the p-Si core, respectively. The shell growth time is 15 min.

substitutional sites of Ge atoms in the n-Ge shell of i-Si/n-Ge core−shell NWs. The Ge optical phonon peak shows a slightly asymmetric broadening toward lower wavenumbers, most likely resulting from the Fano effect,[23,26,27] which is due to the coupling between discrete optical phonons and the continuum of interband electron excitations in degenerately doped n-type Ge. The Fano interference shows the electrical activity of P atoms in the substitutional sites of Ge atoms in the n-Ge shell. On the other hand, no asymmetric broadening or P local vibrational peak were observed for p-Si/i-Ge core−shell NWs, as shown in Figure 6c. On the basis of these results, we can clearly show P donor doping in the n-Ge shell of i-Si/n-Ge core−shell NWs. Figure 6f shows the results for i-Ge/p-Si. Here, the samples had to be annealed at 900 °C for 30 s. The results of TEM, XRD, and Raman show that the Si shell is almost a perfect crystal, but higher temperature annealing was needed to electrically fully activate the B dopant atoms in the Si shell. This is due to the enhancement of radial growth by adding the B_2H_6 gas. Two peaks were observed at about 618 and 640 cm^{-1} as shown in Figure 6g. These are assigned to the local vibrational modes of the two isotopes of ^{11}B (80.2%) and ^{10}B (19.8%) in the Si.[28,29] We also observed an asymmetric broadening to a higher wavenumber, which is a characteristic of highly B-doped Si. This is due to the Fano effect. No asymmetric broadening and B local vibrational peaks were observed in n-Ge/i-Si core−shell NWs shown in Figure 6h. These results clearly show that B atoms are located at numerous Si atom sites and are electrically activated at these sites, demonstrating B-acceptor doping in the p-Si shell in i-Ge/p-Si core−shell NWs. As for impurity doping in the core regions, we can obtain proof by analyzing the sample before shell growth. The results of B doping in SiNWs are shown in Figure 6 panels d and e. The results of P doping in GeNWs are shown in Figures 6i and 6j. P doping in the Ge core region has also been reported in our previous results describing P-doping in GeNWs.[23] Hence, we can use Raman analysis to show the selective doping of B and P in Si/Ge and Ge/Si core−shell NWs. We also analyzed the Ge and the Si optical phonon peaks using the Fano equation.[26] The asymmetric line shape of the phonon is given by

$$I(\omega) = I_0 \frac{(q+\varepsilon)^2}{(1+\varepsilon^2)} \quad (1)$$

where ω is the wavenumber, I_0 is the prefactor, q is the asymmetry parameter, and ε is given by $\varepsilon = (\omega - \omega_p)/\Gamma$, where ω_p is the phonon wavenumber and Γ is the line width parameter. The values of q and Γ were estimated to be about −18.0 and 2.8, respectively, for i-Si/n-Ge. On the other hand, the values of q and Γ were estimated to be about 8.8 and 10.5, respectively, for i-Ge/p-Si. From our previous results for P-doped

TABLE 1. Summary of the Fano Parameters and Stress for Si/Ge and Ge/Si Core–Shell Nanowires

	Fano parameters		stress	
	q	Γ	core	shell
i-Si/n-Ge	−18.0	2.8	tensile	compressive
n-Ge/i-Si	−18.1	2.4	compressive	tensile
i-Ge/p-Si	8.8	10.5	compressive	tensile
p-Si/i-Ge	5.2	12.1	tensile	compressive

GeNWs[23] and typical results for B-doped bulk Si,[30−32] the electrically active P and B concentration in the Ge and Si shells can be roughly estimated to be in the order of 10^{19} cm^{-3}. Table 1 shows the summary of the results. According to the previous results by Goldthorpe *et al.*,[12,13] some dislocations can be introduced into the shell regions. Even if some dislocations are introduced into the shell regions, we could achieve high electrical active dopant concentrations, 10^{19} cm^{-3}, in the shell regions. The dopant distribution is also important for device applications. The dopant atoms uniformly distribute in the axial direction in the core regions if the structures of NWs are untapered.[23] On the other hand, they distribute in the radial direction preferentially near the surface regions.[24] This is probably not a serious problem from the viewpoint of introducing carriers from the core to the shell regions. As for the shell regions, dopant atoms must be inhomogeneously distributed in the radial direction due to the effect of stress. Considering future device applications, the thickness of the shell layers should be thin. Therefore the dopant distribution in the radial direction also may not be a serious problem. We verified that the core–shell NWs are untapered in the axial growth direction after shell formation, showing that the axial distribution of dopant atoms in the shell regions is probably almost uniform.

Finally, we discuss the dopant diffusion and the Si–Ge interdiffusion in Ge/Si core–shell NWs. The Si shells were formed at 700 °C for n-Ge/i-Si and i-Ge/p-Si core–shell NWs. The diffusion coefficients of P and B atoms in bulk Si and Ge have been reported by many researchers.[33,34] The diffusion of dopant atoms depends on various conditions, such as process temperature, doping concentration, defect concentration, and strain in Si and Ge. The general agreements between different measurements and samples are thus not always good. For example, the diffusion activation energy and the pre-exponential factor for P in Si have been reported to be 2.74 ± 0.07 eV and (8 ± 5) × 10^{-4} cm^2/s, while the corresponding values for B are 3.12 ± 0.04 eV and (6 ± 2) × 10^{-2} cm^2/s.[35] These values are also in good agreement with results obtained by *ab initio* calculations.[36] On the basis of our experimental conditions, the diffusion coefficients of B and P in Si at 700 °C are roughly in the order of 10^{-17}–10^{-18} cm^2 s^{-1}. The reported values of the diffusion coefficient of B in Ge are significantly scattered: namely, they have in the past been reported to be 10^{-12}–10^{-14} cm^2 s^{-1},[37,38] but more recent readings are in the order of 10^{-16}–10^{-17} cm^2 s^{-1}.[39,40] These more recent values are similar to the corresponding values for B and P in Si. On the other hand, the diffusion coefficient of P in Ge is in the range of 8 × 10^{-13} to 10^{-14} cm^2 s^{-1}, lower than the other above-mentioned values.[41−43] In the case of n-Ge/i-Si core–shell NWs, P diffusion is possible in the n-Ge core at 700 °C for 15 min, but diffusion to the i-Si shell is virtually zero, due to the low diffusivity of P in Si (less than 1 nm diffusion length). The diffusion of B atoms from the shell to the core in the i-Ge/p-Si core–shell NWs is also negligible, since the diffusion length of B atoms is in the same order of that of P atoms in Si. The dopant diffusion in the Si/Ge core–shell NWs is much more difficult than in the above-mentioned Ge/Si (n-Ge/i-Si and i-Ge/p-Si) core–shell NWs. This is because the shell growth temperature is 600 °C for the Si/Ge core–shell NWs, lower than that of the Ge/Si core–shell NWs. Hence, the dopant diffusion is close to zero in both cases. However, the interdiffusion of Si and Ge during shell growth at 700 °C should be taken into account. The diffusion coefficient of Ge in Si at 700 °C is lower than 10^{-18} cm^2 s^{-1}, while that of Si in Ge is in the order of 10^{-15} to 10^{-16} cm^2 s^{-1}.[44−46] The diffusion of Ge atoms into Si is virtually zero. However, it is possible for Si atoms to diffuse as far as 10 nm at 700 °C in 15 min. This estimation indicates that the intermixing of Si and Ge might occur, but only at the interface of the Ge/Si core–shell NWs; and if this were to happen, dopant diffusion might occur, but it would be limited to the interface. We investigated the structure of core–shell NWs using EDX measurements, but, due to low resolution, it was close to impossible to obtain the interdiffusion signature. If core–shell NWs are being considered for use in nanodevices, this interdiffusion of Si and Ge, and that of dopant atoms will be crucial problems, since they affect the abruptness of the band offset at the Si/Ge interface.

CONCLUSION

The growth of Si/Ge and Ge/Si core–shell NWs and site-selective doping within them were carried out by CVD. XRD and micro-Raman measurements clearly revealed stress in the core and shell regions and characterized the compressive and tensile stress present. The formation of the Ge shell applies tensile stress to the Si core, while the Si core applies compressive stress to the Ge shell. Conversely, the formation of the Si shell applies compressive stress on the Ge core, while the Ge core applies tensile stress to the Si shell. XRD and micro-Raman measurements also clearly demonstrated site-selective doping. XRD revealed peak shifts

due to lattice contraction caused by doping with P and B atoms. The local vibrational peaks of P and B atoms and Fano broadening in the optical phonon peaks were observed using Raman scattering methods that showed the p and n-shells in the Si/Ge and Ge/Si core–shell NWs.

EXPERIMENTAL METHODS

Core–shell Si/Ge and Ge/Si nanowires were grown on a Si (111) substrate by chemical vapor deposition (CVD). Gold nanocolloid particles of 3 nm in diameter were used as seeds for vapor–liquid–solid (VLS) growth[47] of core-SiNWs and core-GeNWs using 19 sccm of SiH_4 (100%) and 10 sccm GeH_4 (100%), respectively. The total pressure was set at 8 Torr by mixing with N_2 gas. Doping with B and P was mainly performed during the VLS growth. Doping by surface deposition can also be considered especially for the B doping.[23] Diborane (1% B_2H_6 in H_2) was used for the p-type dopant and phosphine (1% PH_3 in H_2) for the n-type dopant. Four different types of core–shell nanowires were grown. The first structure was intrinsic-Si/n-type-Ge (i-Si/n-Ge) core–shell nanowires. The axial growth of i-SiNWs was performed at 550 °C for 10 min and the subsequent radial growth of the n-Ge shell layer was achieved at 500 °C using 7 sccm of PH_3. Here, we once decreased the temperature up to room temperature in the CVD chamber before the shell growth process. This process is effective to retard the axial growth during the shell formation. In addition to this, PH_3 gas was introduced in advance of the shell growth. This process also suppresses the axial growth by the VLS process. The similar processes were also done for the other three different core–shell NWs described below. The difference is that the B_2H_6 gas was used for the third and fourth structure instead of PH_3 gas. The second structure was n-Ge/i-Si core–shell nanowires. The n-GeNWs were grown at 300 °C for 15 min using 0.5 sccm of PH_3 and the i-Si shell layer was formed at 700 °C. The third structure was p-Si/i-Ge core–shell nanowires. The p-SiNWs were grown at 550 °C for 10 min using 0.2 sccm of B_2H_6 and the i-Ge shell layer was formed at 500 °C. The last structure was i-Ge/p-Si core–shell nanowires. The i-GeNWs were grown at 300 °C for 15 min and p-Si shell layers were formed at 700 °C using 2 sccm of B_2H_6. Here, the dopant gas flux during the growth of core NWs was lower than that for the shell growth to suppress any tapered structures that might result from surface deposition during core growth. A clear interface between Si and Ge without oxidation was obtained, since the background pressure in our CVD chamber was about 2×10^{-6} Pa.

Scanning electron microscopy (SEM) and TEM were used to observe the core–shell NWs and to investigate the details of their structures. Energy-dispersive X-ray analysis (EDX) measurements were also performed during TEM to investigate the chemical content of the core–shell NWs. X-ray diffraction (XRD) measurements (Cu Kα radiation) were performed to investigate individually the stress in the core and shell regions. The XRD data were collected with parallel beam geometry. Micro-Raman scattering measurements were also performed to investigate the stress in the core–shell NWs, at room temperature using a 100× objective and a 532-nm excitation light source. These methods were also used to clarify the states of dopant atoms, and finally the B and P doping in the shell region. The excitation power was set at about 0.02 mW to prevent local heating effects by the excitation laser.[48–50] The spectral resolution of all data was about 0.3 cm^{-1}.

Conflict of Interest: The authors declare no competing financial interest.

Acknowledgment. This work was in part supported by a Funding Program for Next Generation World-Leading Researchers (NEXT Program), Japan, and the World Premier International Research Center Initiative (WPI Initiative), MEXT, Japan. This study was also supported by the Japan Science and Technology Agency (JST).

Supporting Information Available: Optical phonon peaks related to Si–Ge bonds. This material is available free of charge *via* the Internet at http://pubs.acs.org.

REFERENCES AND NOTES

1. Li, Y.; Qian, F.; Lieber, C. M. Nanowire Electronic and Optoelectronic Devices. *Mater. Today* **2006**, *9*, 18–27.
2. Thelander, C.; Agarwal, P.; Brongersma, S.; Eymery, J.; Feiner, L. F.; Forchel, A.; Scheffler, M.; Riess, W.; Ohlsson, B. J.; Gösele, U.; Samuelson, L. Nanowire-Based One-Dimensional Electronics. *Mater. Today* **2006**, *9*, 28–35.
3. Pauzauskie, P. J.; Yang, P. Nanowire Photonics. *Mater. Today* **2006**, *9*, 36–45.
4. Fan, H. J.; Werner, P.; Zacharias, M. Semiconductor Nanowires: From Self-Organization to Patterned Growth. *Small* **2006**, *2*, 700–717.
5. Wang, Z. L.; Song, J. Piezoelectric Nanogenerators Based on Zinc Oxide Nanowire Arrays. *Science* **2006**, *312*, 242–246.
6. Chockla, A. M.; Korgel, B. A. Seeded Germanium Nanowire Synthesis in Solution. *J. Mater. Chem.* **2009**, *19*, 996–1001.
7. Perea, D. E.; Hemesath, E. R.; Schwalbach, E. J.; Lensch-Falk, J. L.; Voorhees, P. W.; Lauhon, L. J. Direct Measurement of Dopant Distribution in an Individual Vapour–Liquid–Solid Nanowire. *Nat. Nanotechnol.* **2009**, *4*, 315–319.
8. Bierman, Matthew J.; Lau, Y.K. Albert; Kvit, Alexander V.; Schmitt, Andrew L.; Jin, Song Dislocation-Driven Nanowire Growth and Eshelby Twist. *Science* **2008**, *320*, 1060–1063.
9. Lauhon, L. J.; Gudiksen, M. S.; Wang, D.; Lieber, C. M. Core–Multishell Nanowire Heterostructures. *Nature* **2002**, *420*, 57–61.
10. Musin, R. N.; Wang, X. Q. Structural and Electronic Properties of Epitaxial Core–Shell Nanowire Heterostructures. *Phys. Rev. B* **2005**, *71*, 155318.
11. Xiang, J.; Lu, W.; Hu, Y.; Wu, Y.; Yan, H.; Lieber, C. M. Ge/Si Nanowire Heterostructures As High-Performance Field-Effect Transistors. *Nature* **2006**, *441*, 489–493.
12. Goldthorpe, I. A.; Marshall, A. F.; McIntyre, P. C. Synthesis and Strain Relaxation of Ge-Core/Si-Shell Nanowire Arrays. *Nano Lett.* **2008**, *8*, 4081–4086.
13. Goldthorpe, I. A.; Marshall, A. F.; McIntyre, P. C. Inhibiting Strain-Induced Surface Roughening: Dislocation-Free Ge/Si and Ge/SiGe Core-Shell Nanowires. *Nano Lett.* **2009**, *9*, 3715–3719.
14. Swadener, J. G.; Picraux, S. T. Strain Distributions and Electronic Property Modifications in Si/Ge Axial Nanowire Heterostructures. *J. Appl. Phys.* **2009**, *105*, 044310.
15. Park, J.-S.; Ryu, B.; Moon, C.-Y.; Chang, K. J. Defects Responsible for the Hole Gas in Ge/Si Core–Shell Nanowires. *Nano Lett.* **2010**, *10*, 116–121.
16. Li, L.; Smith, D. J.; Dailey, E. Madras, P.; Drucker, J.; Mccartney, M. R. Observation of Hole Accumulation in Ge/Si Core/Shell Nanowires Using Off-Axis Electron Holography. *Nano Lett.* **2011**, *11*, 493–497.
17. Amato, M.; Ossicini, S.; Rurali, R. Band-Offset Driven Efficiency of the Doping of SiGe Core-Shell Nanowires. *Nano Lett.* **2011**, *11*, 594–598.
18. Zhao, Y.; Smith, J. T.; Appenzeller, J.; Yang, C. Transport Modulation in Ge/Si Core/Shell Nanowires through Controlled Synthesis of Doped Si Shells. *Nano Lett.* **2011**, *11*, 1406–1411.
19. Dayeh, S. A.; Wang, J.; Li, N.; Huang, J. Y.; Gin, A. V.; Picraux, S. T. Growth, Defect Formation, and Morphology Control of Germanium_Silicon Semiconductor Nanowire Heterostructures. *Nano Lett.* **2011**, *11*, 4200–4206.

20. Oberhuber, R.; Zandler, G.; Vogl, P. Subband Structure and Mobility of Two-Dimensional Holes in Strained Si/SiGe MOSFET's. *Phys. Rev. B* **1998**, *58*, 9941–9948.
21. Fischetti, M. V.; Ren, Z.; Solomon, P. M.; Yang, M.; Rim., K. Six-Band k·p Calculation of the Hole Mobility in Silicon Inversion Layers: Dependence on Surface Orientation, Strain, And Silicon Thickness. *J. Appl. Phys.* **2003**, *94*, 1079–1095.
22. Fukata, N. Impurity Doping in Silicon Nanowires. *Adv. Mater.* **2009**, *21*, 2829–2832.
23. Fukata, N.; Sato, K.; Mitome, M.; Bando, Y.; Sekiguchi, T.; Kirkham, M; Hong, J. I.; Wang, Z. L.; Snyder, R. L. Doping and Raman Characterization of Boron and Phosphorus Atoms in Germanium Nanowires. *ACS Nano* **2010**, *4*, 3807–3816.
24. Fukata, N.; Ishida, S.; Yokono, S.; Takiguchi, R.; Chen, J.; Sekiguchi, T.; Murakami, K. Segregation Behaviors and Radial Distribution of Dopant Atoms in Silicon Nanowires. *Nano Lett.* **2011**, *11*, 651–656.
25. Schlitz, R. A.; Perea, D. E.; Lensch-falk, J. L.; Hemesath, E. R.; Lauhon, L. J. Correlating Dopant Distributions and Electrical Properties of Boron-Doped Silicon Nanowires. *Appl. Phys. Lett.* **2009**, *95*, 162101.
26. Fano, U. Effects of Configuration Interaction on Intensities and Phase Shifts. *Phys. Rev.* **1961**, *124*, 1866–1878.
27. Olego, D.; Cardona, M. Self-Energy Effects of the Optical Phonons of Heavily Doped *p*-GaAs and *p*-Ge. *Phys. Rev. B* **1981**, *23*, 6592–6602.
28. Herrero, C. P.; Stutzmann, M. Microscopic Structure of Boron−Hydrogen Complexes in Crystalline Silicon. *Phys. Rev. B* **1988**, *38*, 12668–12671.
29. Fukata, N.; Chen, J.; Sekiguchi, T.; Okada, N.; Murakami, K.; Tsurui, T.; Ito, S. Doping and Hydrogen Passivation of B in Silicon Nanowires Synthesized by Laser Ablation. *Appl. Phys. Lett.* **2006**, *89*, 203109.
30. Cerdeira, F.; Fjeldly, T. A.; Cardona, M. Effect of Free Carriers on Zone-Center Vibrational Modes in Heavily Doped *p*-type Si. II. Optical Modes. *Phys. Rev. B* **1973**, *8*, 4734–4745.
31. Arya, K.; Kanehisa, M. A.; Jouanne, M.; Jain, K. P.; Balkanski, M. Pseudopotential Calculation of the Discrete-Continuum Interference in p-Si Raman Spectra. *J. Phys. C: Solid State Phys.* **1979**, *12*, 3843–3853.
32. Chandrasekhar, M.; Chandrasekhar, H. R.; Grimsditch, M.; Cardona., M. Study of the Localized Vibrations of Boron in Heavily Doped Si. *Phys. Rev. B.* **1980**, *22*, 4825–4833.
33. Fahey, P. M.; Griffin, P. B.; Plummer, J. D. Point Defects and Dopant Diffusion in Silicon. *Rev. Mod. Phys.* **1988**, *61*, 289–384.
34. Sharma, L. Diffusion in Silicon and Germanium. *Defect Diff. Forum* **1990**, *70−71*, 1–102.
35. Cristensen, J. S.; Radamson, H. H.; Kuznetsov, A. Yu.; Svensson, B. G. Phosphorus and Boron Diffusion in Silicon under Equilibrium Conditions. *Appl. Phys. Lett.* **2003**, *82*, 2254–2256.
36. Ma, S. Y.; Wang, S. Q. *Ab Initio* Calculation of Intrinsic Diffusion Coefficients for Boron in Silicon at Finite Temperatures. *Eur. Phys. J. B* **2009**, *72*, 567–573.
37. Dunlap, W. C., Jr. Diffusion of Impurities in Geirnanium. *Phys. Rev.* **1954**, *94*, 1531–1540.
38. Meer, W.; Pommerrenig, D. *Z. Angew. Phys.* **1967**, *23*, 369.
39. Uppal, S.; Willoughby, Arthur F. W.; Bonar, J. M.; Evans, A. G.; Cowen, Nick E. B.; Morris, R.; Dowsett, M. G. Diffusion of Ion-Implanted Boron in Germanium. *J. Appl. Phys.* **2001**, *90*, 4293–4295.
40. Uppal, S.; Willoughby, Arthur F. W.; Bonar, J. M.; Cowen, Nick E. B.; Grasby, T.; Morris, Richard J. H.; Dowsett, M. G. Diffusion of Boron in Germanium at 800−900 °C. *J. Appl. Phys.* **2004**, *96*, 1376–1380.
41. Matsumoto, S.; Niimi, T. Concentration Dependence of a Diffusion Coefficient at Phosphorus Diffusion in Germanium. *J. Electrochem. Soc.* **1978**, *125*, 1307–1309.
42. Chui, C. O.; Gopalakrishnan, K.; Griffin, P. B.; Plummer, J. D.; Saraswat, K. C. Activation and Diffusion Studies of Ion-Implanted p and n Dopants in Germanium. *Appl. Phys. Lett.* **2003**, *83*), 3275–3277.
43. Canneaux, T.; Mathiot, D.; Ponpon, J. P.; Leroy, Y. Modeling of Phosphorus Diffusion in Ge Accounting for a Cubic Dependence of the Diffusivity with the Electron Concentration. *Thin Solid Films* **2010**, *518*, 2394–2397.
44. Silvestri, H. H.; Bracht, H.; Hansen, J. L.; Larsen, A. N.; Haller, E. E. Diffusion of Silicon in Crystalline Germanium. *Semicond. Sci. Technol.* **2006**, *21*, 758–762.
45. Gavelle, M.; Bazizi, E. M.; Scheid, E.; Fazzini, P. F.; Cristiano, F.; Armand, C.; Lerch, W.; Paul, S.; Campidelli, Y.; Halimaoui, A. Detailed Investigation of Ge−si Interdiffusion in the Full Range of $Si_{1-x}Ge_x$ ($0 \leq x \leq 1$) Composition. *J. Appl. Phys.* **2008**, *104*, 113524.
46. Castrillo, P.; Pinacho, R.; Jaraiz, M.; Rubio, J. E. Physical Modeling and Implementation Scheme of Native Defect Diffusion and Interdiffusion in SiGe Heterostructures for Atomistic Process Simulation. *J. Appl. Phys.* **2011**, *109*, 103502.
47. Wagner, R. S.; Ellis, W. C. Vapor−Liquid−Solid Mechanism of Single Crystal Growth. *Appl. Phys. Lett.* **1964**, *4*, 89–90.
48. Piscanec, S; Cantoro, M; Ferrari, A. C.; Zapien, J. A.; Lifshitz, Y.; Lee, S. T.; Hofmann, S.; Robertson., J. Raman Spectroscopy of Silicon Nanowires. *Phys. Rev. B* **2003**, *68*, 241312(R).
49. Fukata, N.; Oshima, T.; Murakami, K.; Kizuka, T.; Tsurui, T.; Ito, S. Phonon Confinement Effect of Silicon Nanowires Synthesized by Laser Ablation. *Appl. Phys. Lett.* **2005**, *86*, 213112.
50. Fukata, N.; Oshima, T.; Okada, N.; Kizuka, T.; Tsurui, T.; Ito, S.; Murakami, K. Phonon Confinement and Self-Limiting Oxidation Effect of Silicon Nanowires Synthesized by Laser Ablation. *J. Appl. Phys.* **2006**, *100*, 024311.